J. Fluid Mech. (1989), *vol.* 203, *pp.* 425–448
Printed in Great Britain

Organized motions in a fully developed turbulent axisymmetric jet

By JIN TSO† AND FAZLE HUSSAIN
Department of Mechanical Engineering, University of Houston, TX 77004, USA

(Received 12 August 1987 and in revised form 5 December 1988)

An experiment has been conducted to study the occurrence, configuration and dynamics of large-scale coherent vortical motions in the fully developed region of a turbulent axisymmetric jet. The key idea is to use vorticity signals from a spatial grid to detect and sample large-scale vortical structures and then use the (smoothed) vorticity peaks of spatial vorticity patterns to align and ensemble average successive realizations to determine structure configuration and dynamics. Measurements were made in an air jet at $Re_D = 69000$ by employing a radial rake of seven $\times$-wires to obtain the azimuthal vorticity map. Two additional conditioning probes were placed $\pm 90°$ away from the rake to determine the three-dimensional phase and hence the structure configuration. Structures with axisymmetric, helical and double helical configurations have been educed. Among them, the helical structures are far more dominant than the others, and the jet dynamics are thus discussed in terms of these helical structures. Helical structures move radially outward as they advect downstream. This radial movement, in conjunction with simultaneous local ejection of turbulent fluid and subsequent entrainment of the ejected fluid with ambient fluid, appears to be a major means of jet spreading. The shear strain rate is strong on the downstream side of the structure, causing intense small-scale turbulence production and mixing there.

1. Introduction

While considerable progress has been made toward understanding coherent motions in the transitional region of the turbulent axisymmetric jet, little is known about their nature, even occurrence, in the fully developed region. The explanation for this can be traced to the fact that previous measurement techniques, though successful in revealing and quantifying the coherent motions in the transitional region, were inappropriate in the fully developed region. The extensively applied controlled excitation methods (Crow & Champagne 1971; Kibens 1980; Zaman & Hussain 1980; Strange & Crighton 1983) were unable to control the organized motions beyond the jet potential core, and smoke and dye visualizations in the fully turbulent region reveal no identifiable organized structures. A new method was clearly needed.

The existence of coherent motions in the fully developed turbulent axisymmetric jet has been suspected by researchers probably ever since coherent motion became the major focus of experimental turbulence research. Conventional time-mean measurements like the wavenumber–celerity spectrum (Hussain & Clark 1981*a*) and the two-point space–time correlations of longitudinal velocity fluctuations (Tso,

† Present address: Aeronautical Engineering Department, California Polytechnic State University, San Luis Obispo, CA 93407, USA.

Kovasznay & Hussain 1981) suggested the occurrence of these motions. Fourier analysis of the conventional azimuthal correlations of both velocity and temperature signals (Tso 1983; Sreenivasan 1984) indicated the azimuthal coherence of flow events. These results however are not conclusive because of the limitations in applying the conventional time-mean methods to study time-dependent coherent motions (Hussain 1980; Lumley 1981; Cantwell 1981; Coles 1981).

The limitations of such conventional measurements in the jet far field can be partially overcome by emerging sophisticated measurement techniques such as particle displacement velocimetry and image processing. Another possibility is smoke or dye visualizations. In one particular example, flow pictures using the laser fluorescence dye technique (Dimotakis, Miake-lye & Papantoniou 1983) showed zigzag flow patterns in one diametral plane at $Re_D = 2500$ (Re_D is the Reynolds number $U_e D/\nu$, where U_e is the jet exit velocity, D the nozzle diameter, and ν the kinematic viscosity), but symmetric flow patterns at $Re_D = 650$. Based on these patterns, the existence of coherent motion in the far field, either of an axisymmetric or a helical configuration, was suggested. However, some further questions remain. First, in the flow pictures obtained, large-scale vortical structures are not clear. Second, the three-dimensional helical structure configuration cannot be evident or unique from the view in a two-dimensional plane. And third, the Reynolds numbers are low; both axisymmetric and sinuous disturbances are known to occur in a range of Reynolds numbers up to 300 (Reynolds 1962). Also, while flow visualization has helped the understanding of the flow physics, it is useful only for short times or distances following injection of dye or smoke. In any case, these flow visualization techniques can only provide qualitative perceptions of organized motions. Therefore, in order to ascertain whether coherent motions occur in the fully developed region, and to determine their configurations and dynamical significance, especially in a high-Reynolds-number jet (say for $Re_D > 10^4$), further investigations involving quantitative information were needed.

The present investigation has thus focused on developing a method that can verify the occurrence of large-scale vortical structures and at the same time determine their configurations and dynamical roles. This was accomplished by the use of a radial, linear rake of $\times$-wires to measure the azimuthal vorticity in the diametral plane (i.e. (x, r)-plane) passing through the $\times$-wire rake. To determine the three-dimensional configurations of the structures, two single-wire probes were placed at the half-radius positions at azimuthal angles $\pm 90°$ away from the rake.

Unlike the nominally two-dimensional structures in plane or axisymmetric mixing layers, most organized structures in the fully developed turbulent axisymmetric jet are three-dimensional. Exploratory tests suggested that, in the far field of an axisymmetric jet, the structures are typically helical – apparently not inconsistent with the stability analysis of Batchelor & Gill (1962). It was clear that the new detection scheme must be capable of addressing the helical configurations of structures and thus had to be more sophisticated than those used for two-dimensional structures. We shall address the helical configurations and their detection methods in §3, before discussing results in §4.

2. Experimental procedures

2.1. *Apparatus and instrumentation*

The experiment was conducted at 50 and 100 diameters downstream of a 2.54 cm circular jet, housed in a $16 \times 32 \times 4$ m laboratory with controlled temperature and

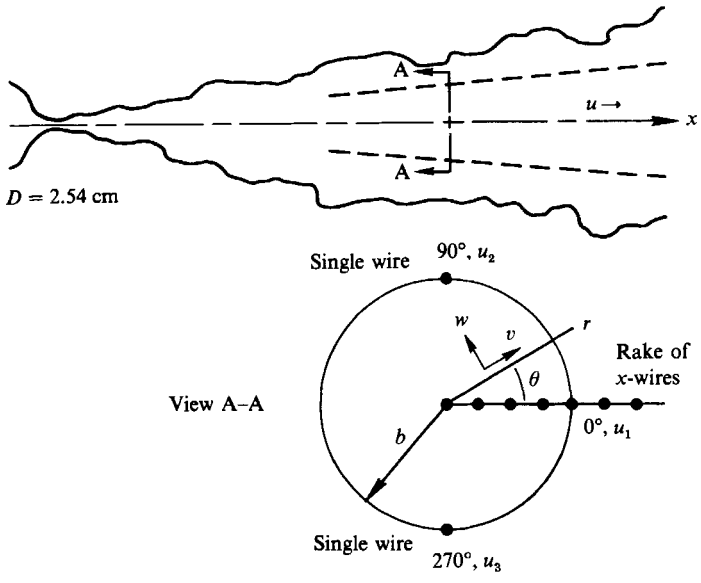

FIGURE 1. Experimental set-up for the conditional sampling scheme.

traffic. The jet, having an initially laminar boundary layer, was studied at an exit velocity of 42 m s^{-1}, corresponding to $Re_D = 69000$. The r.m.s. intensity of longitudinal velocity fluctuations at the jet exit was about 0.1% of the exit velocity. The exit flow had no dominant spectral component.

The velocity signals in this experiment were measured with a custom-made 16-channel anemometer (adapted version of USC-78). Single-wire probes were welded on TSI-1210 sensors with TSI 1150-18 probe supports, and ×-wire probes were welded on TSI-1241 sensors with TSI-1155 probe supports. All these probes used 4 μm tungsten wires operated at an overheat ratio of 0.4.

Signals from the anemometer were sampled using a 12-bit A/D converter (HP9100A) under the control of a laboratory minicomputer (HP2100S). They were used for on-line analysis or stored onto digital magnetic tapes for post-processing. The A/D converter's sampling rate was 20 kHz, and all of its 16 channels were used. The resulting sampling rate of 1.25 kHz per channel is adequate for the large-scale vortical motions studied.

2.2. *Detection scheme*

Vortical motions in the jet far field were studied in this experiment by a novel detection scheme. The experimental set-up is shown in figure 1, along with the cylindrical coordinates r, θ and x. It consists of one rake of seven equally spaced ×-wires aligned radially from the jet centreline to $r = 1.5b$ (b is the local half-radius defined on the basis of the longitudinal mean velocity profile), and two single wires placed at the half-radius positions $\pm 90°$ away from the rake. The spacing between adjacent ×-wires in the rake is $0.25b$; this choice was dictated by the number of ×-wires and a preliminary estimate of the typical size of large-scale vortical motions at the measurement station. The longitudinal velocities at the half-radius positions of 0°, 90° and 270°, denoted by u_1, u_2 and u_3 respectively, were used to infer the structure configuration.

For any two adjacent ×-wires in the rake, the azimuthal vorticity at the point halfway between them was calculated by

$$\Omega \approx \frac{-1}{0.5U_{\mathrm{m}}}\frac{\partial v}{\partial t}-\frac{\partial u}{\partial r}, \tag{1}$$

where U_{m} is the mean velocity at the jet centreline, and u and v are the longitudinal and radial velocities respectively. Taylor's hypothesis with an advection velocity $0.5U_{\mathrm{m}}$ has been used to transform x into t.

Preceding this experiment, the applicability of the Taylor hypothesis to large-scale coherent structures in turbulent shear flows had been evaluated in our laboratory by Zaman & Hussain (1981). Knowing that use of the Taylor hypothesis for studying typical large-scale structures in turbulent shear flows may be grossly in error (Lin 1953), that study was intended to evaluate this error. This was done by comparing the measured actual spatial distributions of the structure properties with those deduced through the use of the hypothesis in the jet transitional region, where the large-scale coherent structures can be stabilized in space and time using controlled excitation. It was observed that the hypothesis works well for an isolated coherent structure if a single advection velocity (i.e. the structure advection velocity) is used across the shear flow. The spatial distributions of the structure properties deduced through the hypothesis were found to be largely the same as the measured actual spatial distributions; the location of the structure 'centre' and the radial extent of the structure were almost identical in both cases, although the vorticity peak magnitudes differed by as much as 15%. A detection scheme using the Taylor hypothesis with a single advection velocity therefore can indicate the passage of large-scale structures, for instance, in the jet far field where the structures are mostly isolated (see §3.1). The study also indicated that the average velocity across the shear region is the optimal choice of the advection velocity. For the mean shear region covered in the present experiment, this average velocity is nearly $0.5U_{\mathrm{m}}$, as already used in (1). Use of the local time-average, phase-average or instantaneous longitudinal velocity as the advection velocity in Taylor's hypothesis, on the other hand, produces unacceptably large distortions. For interacting structures, results also showed that the use of a single advection velocity is the least objectionable.

As to the approximation of $\partial u/\partial r$, the grid size is the radial spacing $0.25b$ between adjacent ×-wires in the rake. For the vortical motions involved in this investigation – the motions whose radial extents are greater than b – this spatial resolution allows at least five vorticity data points in the core region of a sampled structure. This resolution, though not high, is comparable with those employed in other coherent motion studies; see, for example, Browand & Weidman (1976), and Zaman & Hussain (1981). Note that, in some flow situations, the structures are stable in the sense that they occur at the same location at periodic intervals, either because of the low Reynolds number or the use of controlled excitation. Then, a single ×-wire traversing across the shear layer is sufficient to educe structure details by phase-locked measurements, and the spatial resolution can be as fine as the traverse mechanism allows. The random occurrence of the jet far-field structures forced the use of a rake of ×-wires. Since our rake had only seven ×-wires and hence six vorticity data points, the $0.25b$ spacing was the optimum choice for the eduction of large-scale motions.

Once the vorticities were calculated, the detection scheme involved four basic steps (illustrated in figure 2) to select a qualified sample. First, the scheme detected

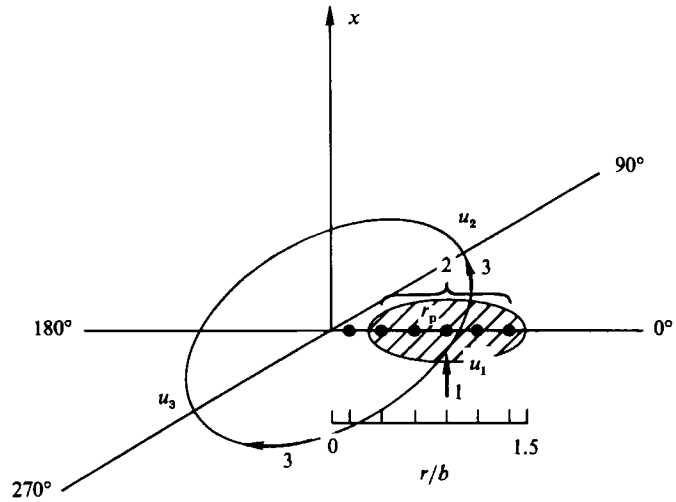

FIGURE 2. Detection steps of the conditional sampling scheme: (1) detect vorticity peak at r_p; (2) examine correlation of vorticities at $r_p-\frac{1}{2}b$ and $r_p+\frac{1}{2}b$; and (3) examine correlations among velocities u_1, u_2 and u_3. The shaded region represents a large-scale vorticity concentration and the black dots its associated vorticity data points.

a strong peak in the (smoothed) vorticity time trace at the radial position $\frac{7}{8}b$, hereafter denoted by r_p, near the centre of the $\times$-wire rake. Second, it examined at the time instant of this peak a short-time correlation (see §2.3) of vorticities obtained at radial positions $\pm 0.5b$ away from r_p and accepted the sample when the correlation value was greater than a specified threshold value. This step in effect ensured that only large-scale motions of radial extent greater than b were sampled. Third, it examined the azimuthal phase relation of each sampled large-scale vortical motion, using the short-time correlations of velocities u_1, u_2 and u_3, to determine the structure azimuthal configuration. When the sample showed a characteristic phase signature (see § 2.4), it was recorded (step four) for further analysis.

Samples of one particular phase signature (i.e. structures of a particular shape) were aligned with respect to the vorticity peak – the phase reference – and ensemble averaged. A flow quantity $Q(r,t)$ of these samples could thus be decomposed into two parts: the ensemble average $\langle Q(r,t)\rangle$ and the residual part $Q_r(r,t)$; i.e.

$$Q(r,t) = \langle Q(r,t)\rangle + Q_r(r,t).$$

By definition, $\langle Q(r,t)\rangle$ represents the coherent part of the motion and $Q_r(r,t)$ the incoherent part.

2.3. *Short-time averages*

In the four detection steps described above, all the correlations are short-time averaged. This short-time averaging process defines an integral value $\hat{Q}(t;\bar{T})$ of a temporal quantity $Q(t)$ as

$$\hat{Q}(t;\bar{T}) = \frac{1}{\bar{T}}\int_{t-\bar{T}/2}^{t+\bar{T}/2} Q(t')\,\mathrm{d}t', \tag{2}$$

where $\bar{T}$ is the variable averaging time interval. This averaging interval was chosen to be comparable with the timescale of large-scale motions such that $\hat{Q}$ is dominated

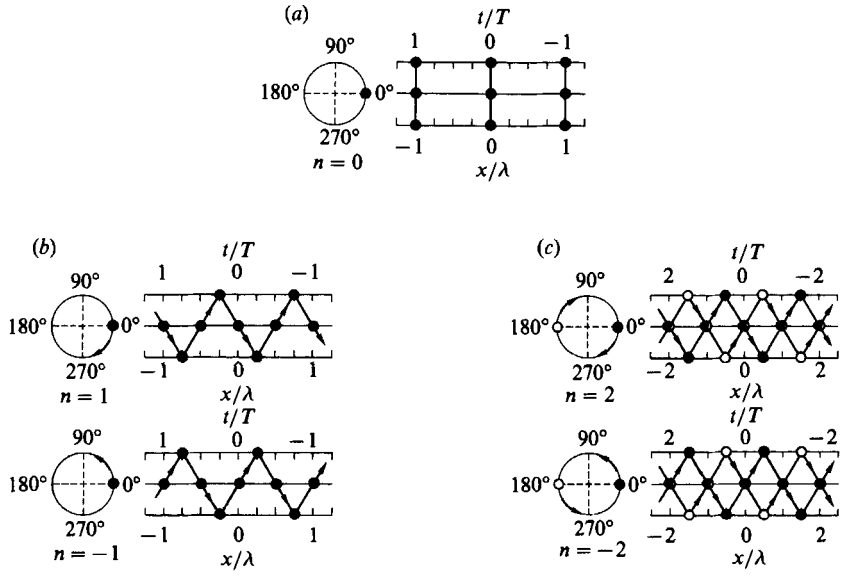

FIGURE 3. Circular helices of normal modes: (*a*) mode 0; (*b*) mode 1; and (*c*) mode 2. The solid line represents the path of the helix and the dots its intersection with the azimuthal locations 0°, 90°, 180° and 270°.

by the low-frequency events (corresponding to large scales). Consequently, this averaging technique helps reveal the organized nature of large-scale motions, as it has done in some earlier works (Gupta, Laufer & Kaplan 1971; Blackwelder & Kaplan 1976). By subtracting the short-time average $\hat{Q}(t;\bar{T})$ from $Q(t)$, a fluctuating variable $q(t;\bar{T})$ is defined, and its (local) r.m.s. value is denoted by $q'(t;\bar{T})$.

Following these definitions, a short-time correlation coefficient of two temporal quantities $q_1(t)$ and $q_2(t)$ at a time delay τ is defined as

$$R(t;\tau,\bar{T}) = \frac{1}{\bar{T}}\int_{t-\bar{T}/2}^{t+\bar{T}/2} q_1(t';\bar{T})\,q_2(t'+\tau;\bar{T})\,\mathrm{d}t' / q_1'(t;\bar{T})\,q_2'(t+\tau;\bar{T}). \tag{3}$$

This correlation is a stochastic quantity with values ranging from -1 to 1. An event can therefore be defined by such correlations, and their joint probabilities have been used in this experiment to educe the azimuthal signatures of vortical motions (see §3.2).

2.4. *Circular helix*

The azimuthal signatures of vortical motions recognized in this experiment match closely the circular helices of normal modes in the jet far field (Batchelor & Gill 1962). For a normal mode disturbance $A(r)\,\mathrm{e}^{\mathrm{i}(n\theta+\alpha(x-ct))}$ (α and n denote the axial and azimuthal wavenumbers and c the phase speed; $\alpha = 2\pi/\lambda$, λ being the wavelength), a helix is a path in space defined by the equations:

$$\alpha x + n\theta = \text{const.}, \quad r = \text{const.} \tag{4a,b}$$

It is a path along which the disturbance has the same phase at any time instant.

For the normal modes 0, 1 and 2 which are most relevant to this study, their circular helices at $r = b$ are illustrated in figure 3. The arrowed solid lines in this figure denote the helices, and the dots are their intersections with azimuthal planes in

increments of 90°. Consider mode +1 as one example. Since $n = 1$ in this case, (4*a*) becomes

$$\theta = -2\pi x/\lambda, \tag{5}$$

where the constant has been set equal to zero by shifting the origin of θ (or x). Thus, as seen in figure 3(*b*), the helix of mode +1 passes $\theta = 0°$ when $x = 0$ and $\theta = 270°$ when $x = \frac{1}{4}\lambda$, and so forth. Since the streamwise coordinate x was converted into time t by using Taylor's hypothesis, the helix has also been plotted against t with a period T replacing the wavelength λ. The cases are similar for the other modes.

This conversion from x into t allows the phase characteristics of normal modes to be described by short-time correlations. In this experiment, they are the correlations among longitudinal velocities u_1, u_2 and u_3 obtained at the half-radius positions of 0°, 90° and 270°(see figure 1). Denote the correlation between u_i and u_j by R_{ij} $(i,j = 1, 2, 3)$. The *out-of-phase* relation of mode +1 at zero time delay, for instance, can thus be denoted by $R_{32}(\tau = 0) = -1$, and its *in-phase* relation along the helix by $R_{31}(\tau = \frac{1}{4}T) = 1$ and $R_{32}(\tau = \frac{1}{2}T) = 1$, etc. (see figure 3*b*). Similar descriptions apply to the other modes.

The exact phase relations characterized by the circular helices, however, can seldom hold in a turbulent jet because structures suffer from jitter in the random environment and have distortions. An ideal correlation peak of value 1 at one in-phase time delay can thus be approximated at most by a correlation peak greater than a threshold value within a time window centred around that time delay. Similarly, an out-of-phase relation can only be indicated by a negative correlation peak less than a negative threshold value. Throughout this experiment, this threshold magnitude, denoted by H, was chosen to be one standard deviation of $R_{32}(\tau = 0)$ above its time mean, and the window size was chosen to be one-eighth of the period between detected structures.

3. Results and discussion

3.1. *Large-scale vortical structures*

The large-scale vortical motions in the jet far field were evident from vorticity contours in the diametral plane passing through the ×-wire rake. Figure 4 shows one such realization obtained at $x/D = 50$, where the jet centreline velocity U_m is 5.1 m s^{-1} and the local half-radius b is 0.11 m. The time axis is plotted from right to left to indicate the occurrence of vortical motions in the physical plane (i.e. x increases to the right). Two contour levels (non-dimensionalized by $|\partial\bar{u}/\partial r|_{max}$) of magnitudes of 1.4 and 2.2 have been drawn in this figure; the solid lines are for the positive contours, and the dashed lines for the negative ones. Note that the structures appear compressed in the streamwise direction in figure 4 as long time traces are used to include more structures per figure.

The vorticity concentrations represented by the contours vary in size, shape, orientation, radial location and strength. Among them, the positive concentrations occur almost everywhere across the mean shear region (radial range covered in the figure). The negative ones, however, occur mostly near the jet centreline. They are presumably the vorticity concentrations which migrate from across the jet centreline, just as some positive ones do the other way too. These vorticity concentrations are mostly isolated, though once in a while they are clustered (as pointed by arrows in figure 4), probably indicating coalescence. They occur less frequently near the outer edge of the jet and seem more dilated in that region. Consequently, the positive

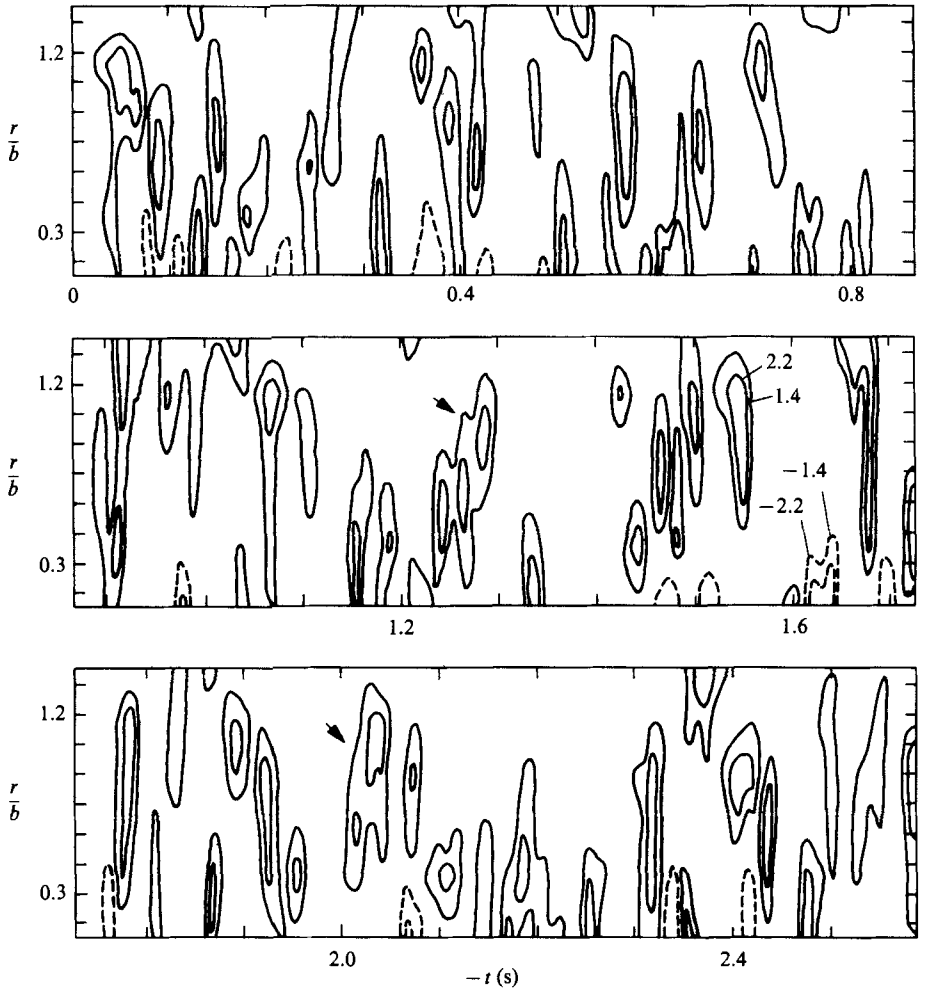

FIGURE 4. Realizations of azimuthal vorticity contours in the (r, t)-plane. Contour levels in sequence are -2.2, -1.4, 1.4 and 2.2. Arrows indicate the clusters of vorticity concentrations.

(solid-lined) vorticity concentrations, or say structures, around the peak mean shear region have been the main focus of further investigation to understand their configurations and transport mechanisms.

In our eduction, a vorticity concentration in the diametral plane was first recorded when the (smoothed) vorticity time trace at r_p had a peak value exceeding its time mean by one standard deviation. The second requirement was that, at the instant of occurrence of this vorticity peak, the short-time correlation of vorticities at radial distances $\frac{1}{2}b$ inside and outside r_p was greater than its time mean by one standard deviation. These two steps together selected a strong vortical structure whose vorticity peak happened to pass by r_p and whose radial extent was greater than b. Actually, for nearly 95% of the samples examined, the vorticity obtained at r_p was greater than vorticities at all other five grid points. Once such a large-scale structure was selected, its configuration (i.e. spatial shape) was subsequently examined by the correlations of longitudinal velocities u_1, u_2 and u_3. These data are explained in the next section.

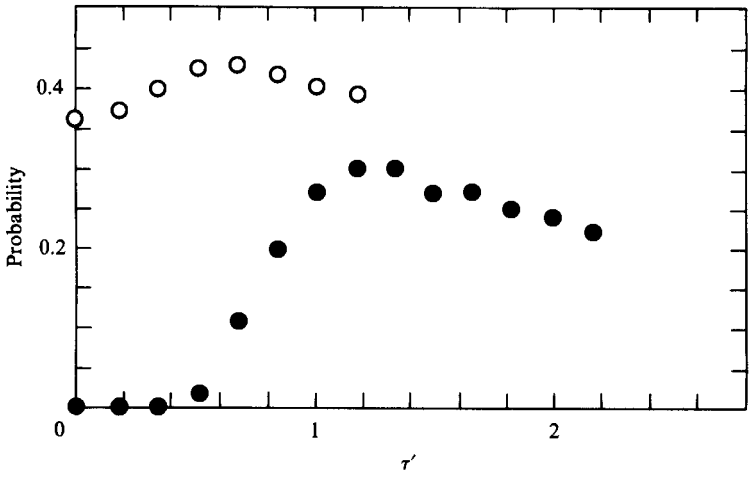

FIGURE 5. Mode 1 signatures of large-scale structures: ○, $R_{31}(\tau) \geqslant H$; ●, $R_{32}(\tau)$ and $R_{32}(-\tau) \geqslant H$.

In computations of these correlations of velocities and vorticities, an averaging time interval of b/U_m was used. It is nearly the time span of a preliminary ensemble-averaged vorticity contour such as those seen in figure 6. Also, the time instants at which the correlations were calculated were those at the vorticity peaks. Therefore, the formal correlation notation $R(t, \tau; \bar{T})$ (see §2.3) is simplified by $R(\tau)$ in later discussions.

3.2. *Structure configurations*

Using the velocity correlations, three types of configurations – namely axisymmetric, helical, and double helical – have been recognized in this investigation. Among them, the helical structures were found to be the most dominant. They will be discussed first.

3.2.1. *Helical structures*

The signatures of helical structures were tested by examining the phase relation between the longitudinal velocities u_2 and u_3 on opposite sides of the jet. Using velocity correlations, we calculated the joint probability of the events when both $R_{32}(\tau)$ and $R_{32}(-\tau)$ for $\tau > 0$ were greater than a threshold H with a simultaneous condition that $R_{32}(\tau = 0)$ was less than $-H$. The result is plotted in figure 5 against the non-dimensional time delay τ', defined as the ratio of the time delay τ over the local timescale $2b/U_m$. The joint probability value is zero at zero time delay because of the out-of-phase condition. It increases with the time delay and reaches a peak at $\tau' \approx 1.2$. This means that when u_2 and u_3 are out of phase at zero time delay, they are most likely to be simultaneously in phase at $\tau' \approx \pm 1.2$.

A similar calculation was performed to determine the in-phase time delay for velocities u_1 and u_3 (of 90° separation). This time, the probability distribution of the event when R_{31} was greater than H was calculated again under the out-of-phase condition at zero time delay. The result, also plotted in figure 5, indicates an in-phase time delay at $\tau' \approx 0.6$, which is one-half the in-phase time delay for u_2 and u_3. This result indicates that when vortical structures pass the detection position, some of them have the azimuthal phase relations characterized by the circular helix of mode

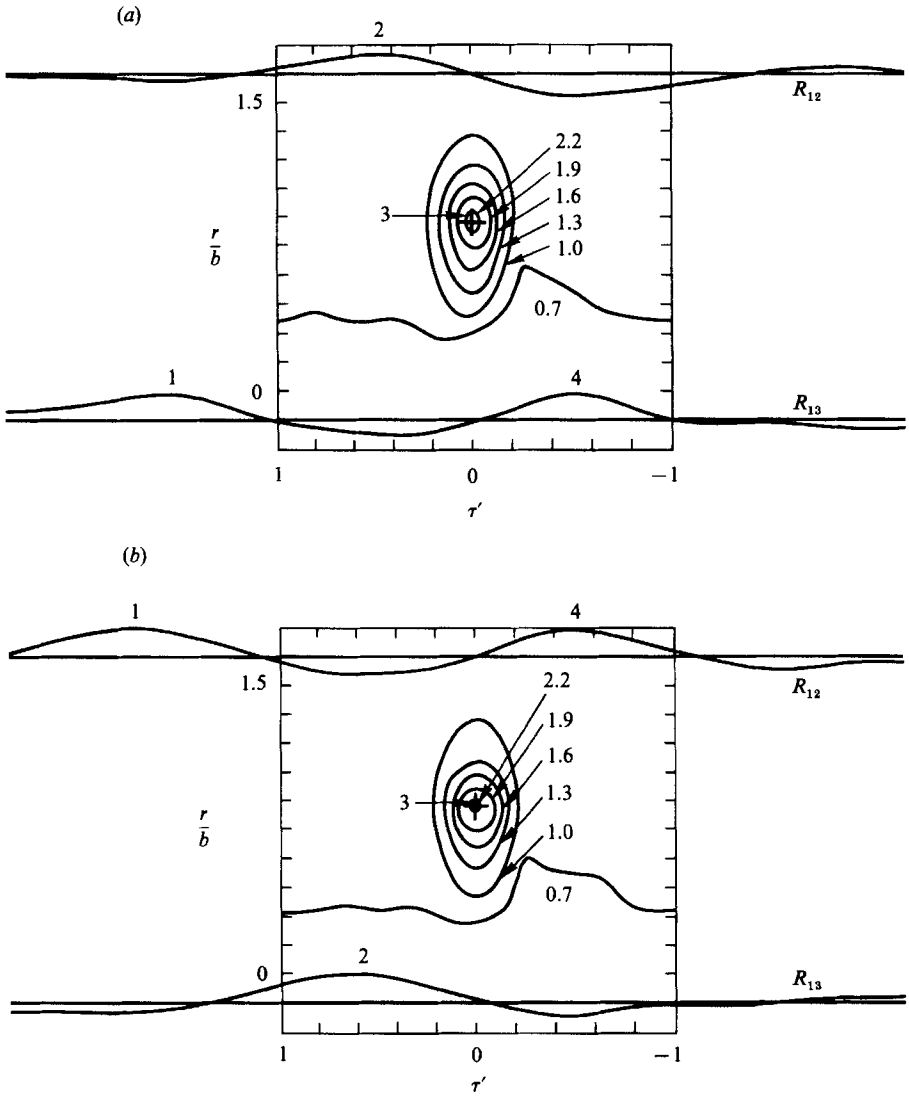

FIGURE 6. Ensemble averages of Ω (non-dimensionalized by $|\partial\bar{u}/\partial r|_{\max}$) and associated $R_{12}(\tau)$ and $R_{13}(\tau)$: (*a*) mode +1; (*b*) mode −1.

+1. That is, when the longitudinal velocities on opposite sides of the jet axis are out-of-phase at zero time delay, their in-phase time delays in both directions of the time axis are twice that for 90° separation. This indicates the occurrence of helical structures in the jet far field. The case is the same for the mode −1 signatures.

For a helical structure, ideally, the correlation between u_1 and u_3 (of 90° separation) at zero time delay should always be zero. Were this the case for all the samples counted in figure 5, none of their velocity correlations would be greater than H and the associated probability value must be equal to zero at $\tau' = 0$. This is not the case in figure 5. This result indicates that if only the out-of-phase condition at zero time delay is used as the eduction criterion, one will sample structures that are either distorted or different from the helical structure. In order to capture the helical structures, therefore, all the in-phase signatures considered in figure 5 (at both 90°

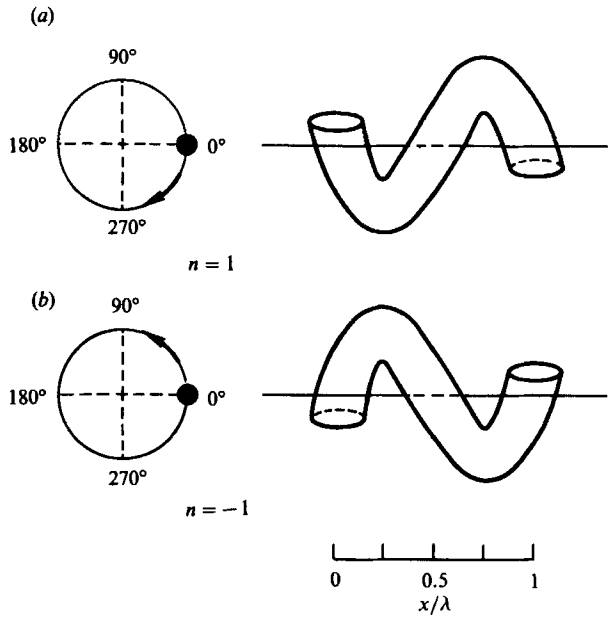

FIGURE 7. Models of helical structures: (*a*) mode +1; (*b*) mode −1.

and 180° azimuthal separations) have been included in the detection, as they should be.

In the sampling process, a large-scale vortical motion is first selected from those samples that have already satisfied the eduction condition at zero time delay. The velocity signal u_1 is then required to be in phase with u_2 at $\tau/T = \frac{1}{4}$ and with u_3 at both $\tau/T = \frac{3}{4}$ and $\tau/T = -\frac{1}{4}$ (see figure 3*b*). T is twice the time delay at which u_2 and u_3 are in phase; it corresponds to the period of the helix shown in figure 3(*b*). Note that the requirement of satisfying the two in-phase conditions at both time delays $\frac{3}{4}T$ and $-\frac{1}{4}T$ at the same azimuthal position (270°) is to ensure that the structure is a helical one (as opposed to other possibilities such as an inclined ring-like structure). In this sampling process, the in-phase condition, as specified in §2.4, is satisfied only when there is a large correlation peak occurring within a time window centred around each detection time delay.

With the vorticity peak as the phase reference, an ensemble average of vorticity was thus obtained from the selected samples along with the two time traces of velocity correlations R_{12} and R_{13}. The results are displayed in figure 6(*a*), where the vortical structure is indicated by the educed vorticity contours and the time axis increases from right to left to indicate the structure occurrence in the physical plane (x increases from left to right). In this figure, positive peaks in R_{12} and R_{13} correspond to the in-phase time delay while negative peaks correspond to the out-of-phase relation. They together characterize the mode +1 helical signature of the vortical structures. These structures are modelled by a helical vortex sketched in figure 7(*a*). Similar results for helical structures of mode −1 signature are shown in figures 6(*b*) and 7(*b*).

3.2.2. *Double-helical structures*

A procedure similar to the preceding one was used to test signatures of double-helical structures. This was done by calculating the joint probability of the events

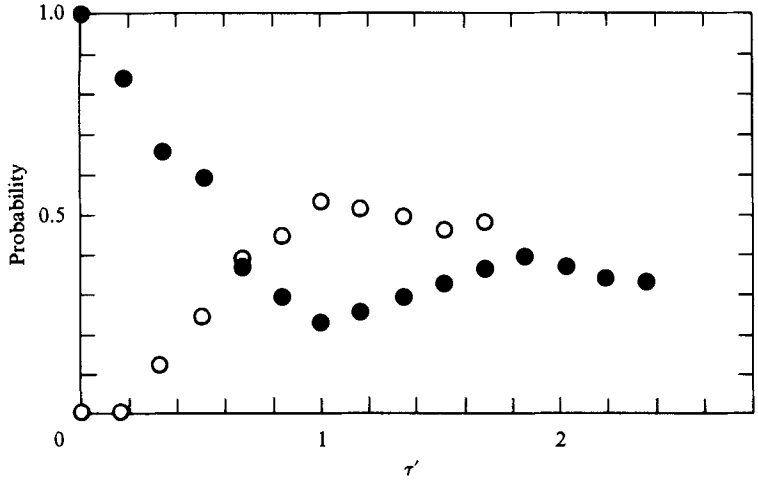

FIGURE 8. Mode 2 signatures of large-scale structures: ○, $R_{31}(\tau) \geqslant H$; ●, $R_{32}(\tau)$ and $R_{32}(-\tau) \geqslant H$.

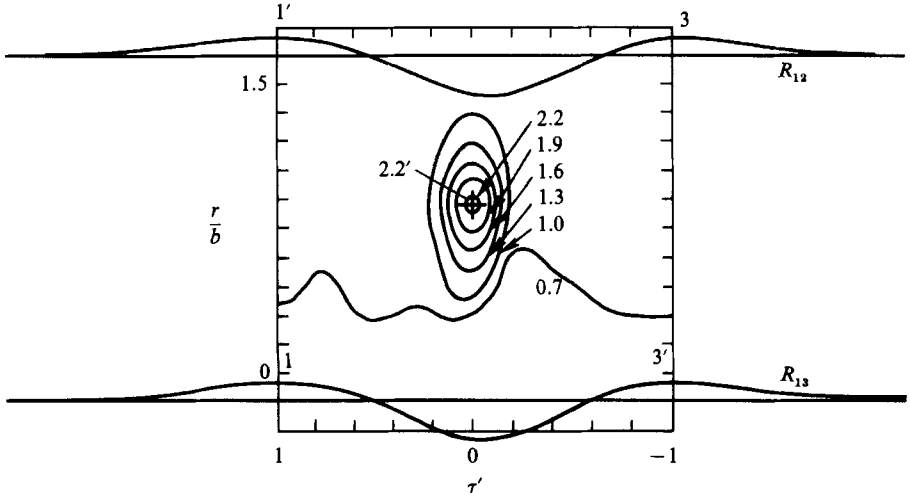

FIGURE 9. Ensemble averages of Ω (non-dimensionalized by $|\partial\bar{u}/\partial r|_{\max}$) and $R_{12}(\tau)$ and $R_{13}(\tau)$ of mode 2.

when both $R_{32}(\tau)$ and $R_{32}(-\tau)$ for $\tau > 0$ were greater than H, with the additional restrictions of the in-phase condition (i.e. $R_{32}(\tau = 0)$ greater than H) and the out-of-phase condition (i.e. $R_{31}(\tau = 0)$ less than $-H$). The result is shown in figure 8. In this figure, the joint probability distribution shows a peak at zero time delay because of the in-phase condition. It shows a second peak at $\tau' \approx 1.9$. On the other hand, the probability for $R_{31}(\tau)$ to exceed H (obtained under the same condition) is zero at zero time delay owing to the out-of-phase condition. Its value increases with the time delay and reaches a peak at $\tau' \approx 1.0$ – a value nearly one-half of 1.9. That is, under the eduction conditions, u_1 and u_3 (of 90° separation) are likely to be in phase at a time delay which is one-half that for u_2 and u_3 (of 180° separation) to be simultaneously in phase in both directions of the time-delay axis. These are the phase

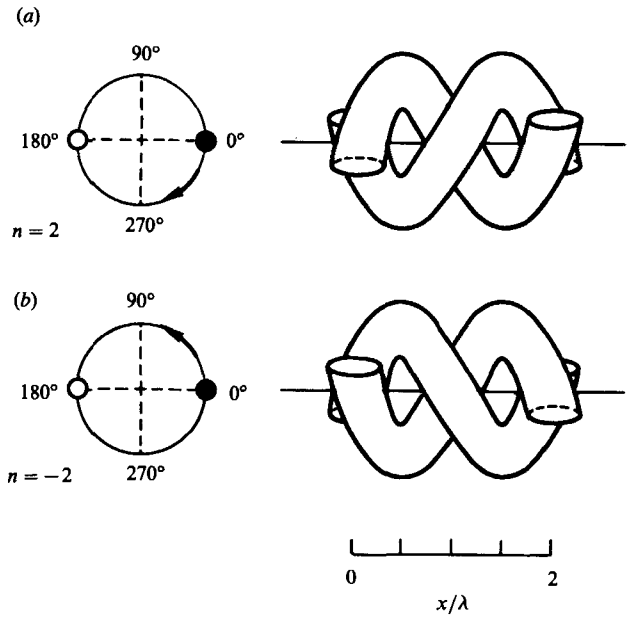

FIGURE 10. Models of double-helical structures of mode 2: (*a*) mode +2; (*b*) mode −2.

characteristics of circular helices of mode 2 shown in figure 3(*c*). They imply the occurrence of double-helical structures in the jet far field.

Vortical structures of mode 2 signatures were selected. For each structure to satisfy the eduction conditions, its velocity u_1 was required to be in phase with u_2 at $\tau/T = \frac{1}{2}$ and u_3 at $\tau/T = -\frac{1}{2}$, or with u_2 at $\tau/T = -\frac{1}{2}$ and u_3 at $\tau/T = \frac{1}{2}$ (see figure 3*c*). T is the time delay at which R_{32} in figure 8 reaches the second peak, corresponding to the period of double helical structures. With these conditions, no distinction was made between mode 2 and mode −2 signatures. From the selected samples, the ensemble averages of vorticity and the time traces of R_{12} and R_{13} were obtained (figure 9). Here, the double-helical signature of the vortical structure is characterized by the two pairs of correlation peaks (indicating in-phase positions) diagonally across the vorticity map. The models of such double helical structures are sketched in figure 10.

3.2.3. *Ring-like structures*

Structures of mode 0 signatures have also been sought with a similar detection procedure. These signatures were tested by calculating the probability distributions of the two events when both R_{31} and R_{32} were greater than H, with the additional conditions that both $R_{31}(\tau = 0)$ and $R_{32}(\tau = 0)$ be greater than H. As shown in figure 11, these two distributions have peaks at $\tau' = 0$ as a result of the two eduction conditions. They both have a second peak at $\tau' \approx 2.0$. These peaks satisfy the phase characteristics of mode 0 in figure 3(*a*). However, when both R_{12} and R_{13} were required to be greater than H at $\tau' = 2.0$, the number of samples became negligible. Even when they were required to be in phase only at zero time delay, the ensemble size was less than one-third of that of mode 1. Consequently, we conclude that axisymmetric vortical structures are not dynamically important in the jet far field, although they are likely to occur sometimes.

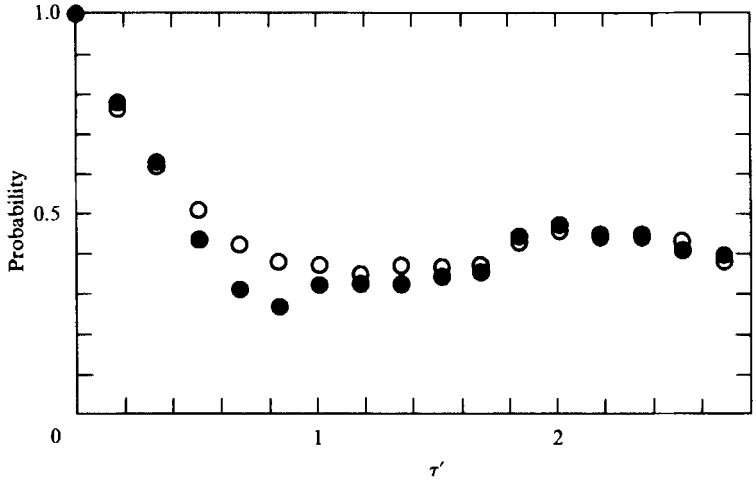

FIGURE 11. Mode 0 signatures of large-scale structures: ○, $R_{31}(\tau) \geqslant H$; ●, $R_{32}(\tau) \geqslant H$.

Azimuthal wave-number n	Time delay τ/T at 90°	Time delay τ/T at 270°
0	0	0
1	$\frac{1}{4}$	$-\frac{1}{4}, \frac{3}{4}$
-1	$-\frac{1}{4}, \frac{3}{4}$	$\frac{1}{4}$
2, -2	$\frac{1}{2}$	$-\frac{1}{2}$
—	$-\frac{1}{2}$	$\frac{1}{2}$

TABLE 1. Detection time delays for modes 0, 1 and 2

3.3. *Dominance of helical structures*

Structures of axisymmetric, helical and double-helical configurations are now recognized. The next task is to determine their importance in jet dynamics, especially in turbulent transport processes. This, however, cannot be done without first knowing the frequency of occurrence of each structure. As discussed earlier and also summarized in table 1, different structures are sampled with different sets of conditions (or restrictions) and, among them, the helical structures have been subjected to the largest number of conditions (three, see §3.2.1) and the longest time delay (i.e. $0.75T$). The use of different conditions for different structures affects the measured frequencies of occurrence.

To illustrate this point, consider the sampling of a mode $+1$ structure. As described in §3.2.1, a mode $+1$ sample is selected when R_{12} at $\tau/T = \frac{1}{4}$ and R_{13} at $\tau/T = \frac{3}{4}$ and $-\frac{1}{4}$ all have peaks greater than the threshold value H within the associated time windows. The window size accounts for phase jitter only in time; no such allowance for radial jitter is included in the detection scheme. For a helical structure passing the detection point, the radial jitter, however, could move its vorticity peak at the 90° position outside the half-radius position while the vorticity peak at 0° (detected at r_p) is still inside the half-radius. Consequently, this helical structure produces a negative R_{12} value and is discarded by the detection scheme. Similar arguments relate to R_{13}. A radial jitter that moves the vorticity peak from $r_p\,(=\frac{7}{8}b)$

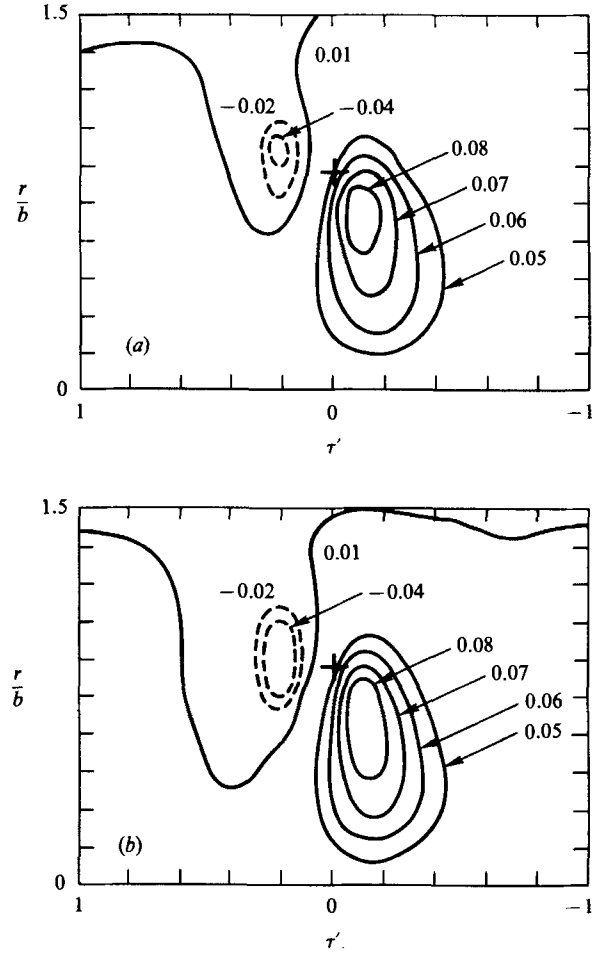

FIGURE 12. Contours of $\langle uv \rangle / U_m^2$: (*a*) mode +1; (*b*) mode −1.

to $r > b$ does not need to be large; it could easily be caused by local incoherent turbulence. The chances for a vorticity peak to occur inside $r = b$ and outside $r = b$ at each of the three detection locations therefore are nearly equal, and the probability of having a positive peak of R_{12} or R_{13} at each detection location is just about one half. (In reality, the vorticity peaks at 90° and 270° were not detected owing to limitations of the number of sensors available; see §2. The probability estimate however should remain unchanged.) As a result, only one-eighth of the desired helical structures should have been sampled.

The samples of helical structures account for about 1.5% of the total sampling time. Following the above argument, one would expect them to occur for 12% of the time. Similarly, mode 2 samples should occur up to 3%, fourfold their actual sampling amount. Thus, the helical structures are far more dominant than all other structures so far recognized in the jet far field. The present conditional sampling scheme detects only those strong and orderly structures whose vorticity peaks happen to pass the detection position r_p. Therefore, structures at other stages of generation and decay, which would be weaker in strength, were not sampled, and structures not centred near r_p were also excluded. Consequently, we believe that the

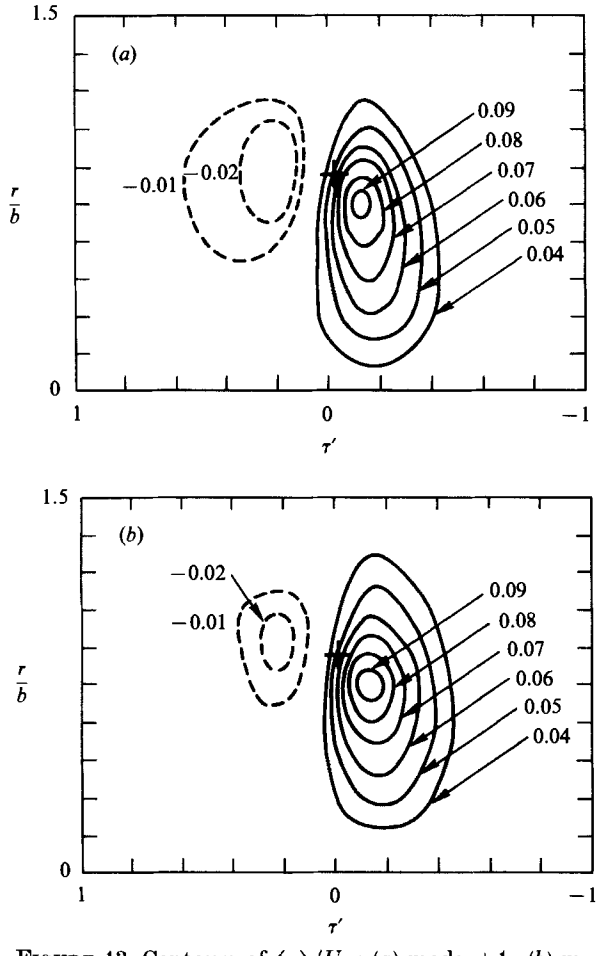

FIGURE 13. Contours of $\langle v \rangle / U_m$: (*a*) mode +1; (*b*) mode −1.

above estimate of the frequency of occurrence of helical structures is conservative. Although large-scale structures other than those discussed so far may indeed be of dynamical significance in the jet far field, none were identified. The following discussion on jet dynamics therefore will be confined to the helical structures.

3.4. *Turbulent transport by helical structures*

3.4.1. *Large-scale momentum transport*

Let us first consider the momentum flux term – the flux of streamwise momentum in the radial direction. This is the most important momentum flux term and is responsible for the spreading of the turbulent axisymmetric jet. The ensemble averages of this quantity, non-dimensionalized by the square of the jet centreline velocity U_m, are shown in figure 12 for both modes +1 and −1. These two averages are fairly close to each other, as expected in the axisymmetric jet. Both figures show a large momentum flux region on the downstream side of the structure; the radial extent of this region is almost the same as that of the structure itself. By contrast, the flux on the upstream side seems less significant.

This result is consistent with the radial velocity distribution $\langle v \rangle$ within the structure. The distribution, which is shown in figure 13 for both modes +1 and −1,

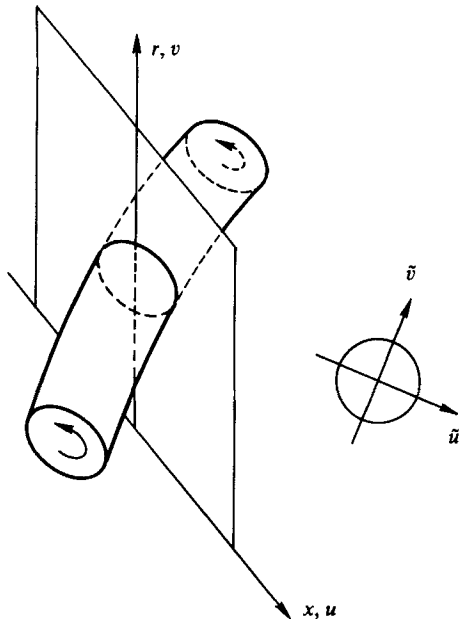

FIGURE 14. Intersection of a single helical structure with one (r,x)-plane.

also possesses a region of strong radial motion on the downstream side. The positive $\langle v \rangle$ region is of roughly the same shape and size as that appearing in $\langle uv \rangle$. As illustrated in figure 14, a helical structure intersects the jet diametral plane at an angle of roughly 60° (determined by $\tan^{-1}(2b/0.5\lambda)$; $\lambda = 0.5U_m T$), and the radial velocity v over the diametral plane should be nearly equal to the radial velocity $\tilde{v}$ over the cross-section of the helical structure. The asymmetry seen in $\langle v \rangle$ therefore should also be seen in $\langle \tilde{v} \rangle$. Physically, this suggests that the vortical structure advects radially outward as a whole. The asymmetry in $\langle v \rangle$ is thus the result of the superposition of the induced radial velocity of the structure and the outward advection. The case for $\langle uv \rangle$ is similar, where the asymmetry in figure 12 should be largely due to the outward momentum transfer associated with this radial advection. Assuming equal induced-velocity peaks on both upstream and downstream sides of the structure in figure 13, the radial advection speed should be around $0.035U_m$. This speed, as noticed, is higher than the radial velocity of about $0.02U_m$ of turbulent bulges reported before by Chevray & Tutu (1978).

As a helical structure moves outward, the ambient fluid at a farther distance from the structure will attain higher induced speed. This has the effect of increasing the engulfment rate and ultimately the jet spreading rate. The jet spreading rate, defined by $\delta b/\delta x$, is near 0.1 in the jet far field. During the time when a structure advects over δx with a speed, say $0.5U_m$, the half-radius b will grow by $0.05U_m \delta t$, where δt is the advection time. Meanwhile, the radial advancement of the structure is about $0.035U_m \delta t$, which is 70% of the half-radius growth. This comparison, though simple, suggests that the radial advection of helical structures can be very important in jet spreading.

Parenthetically, we would like to add that the radial movement *alone does not* achieve all the above effects. For ambient fluid already near the border of a structure, the local ejection of turbulent fluid may also play an important role. This ejection is

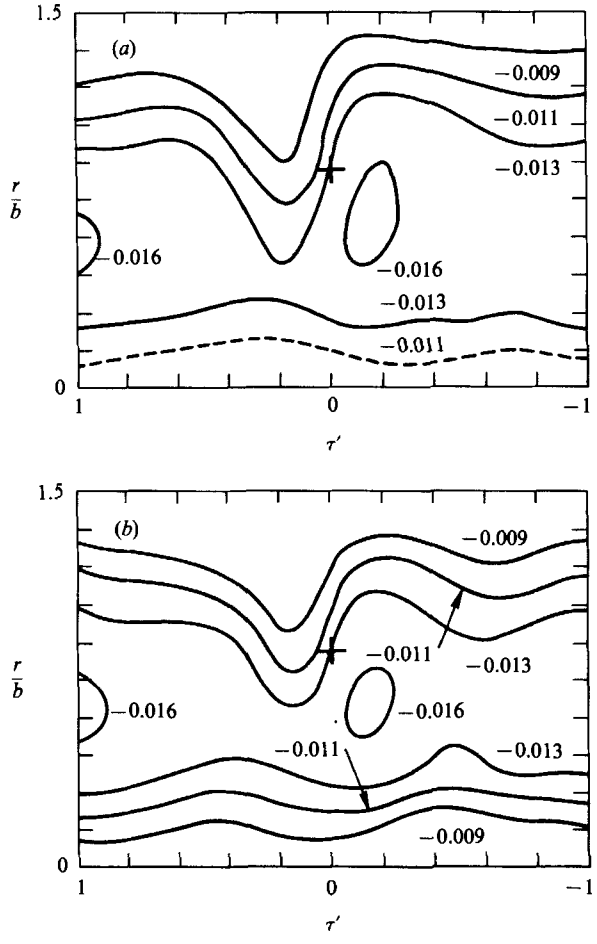

FIGURE 15. Contours of $-\langle u_r v_r \rangle / U_m^2$: (*a*) mode +1; (*b*) mode −1.

mostly local and of mushroom-type, as some flow visualization studies have shown (Hussain & Clark 1981*b*; C. Sinclair & W. Schwarz, private communication 1983). It is perhaps the result of a cut-and-connect process when a part of a vortex folds on itself and pinches off as a vortex ring (Oshima & Asaka 1977). The ejected turbulent fluid, after being shot out and broken down, will mix with ambient fluid in its neighbourhood. This mixture of vortical and non-vortical fluid is later engulfed by the structure as the result of the induced motion of the structure.

3.4.2. *Small-scale mixing*

Small-scale mixing follows large-scale engulfment. In terms of momentum, this process is characterized by the incoherent Reynolds stress term $-\langle u_r v_r \rangle$, plotted in figure 15 for both modes +1 and −1. In both, a peak is seen on the downstream side, near the vorticity peak. This suggests that there is active mixing in that region.

In about the same region where peak $-\langle u_r v_r \rangle$ is observed, the shear strain rate $\langle s \rangle = \frac{1}{2}(\partial\langle v \rangle/\partial x + \partial\langle u \rangle/\partial r)$, which is plotted in figure 16, also shows its highest magnitude. The peak value is about 20% higher than that on the upstream side. Also, the region of large shear strain rate is almost four times that on the upstream

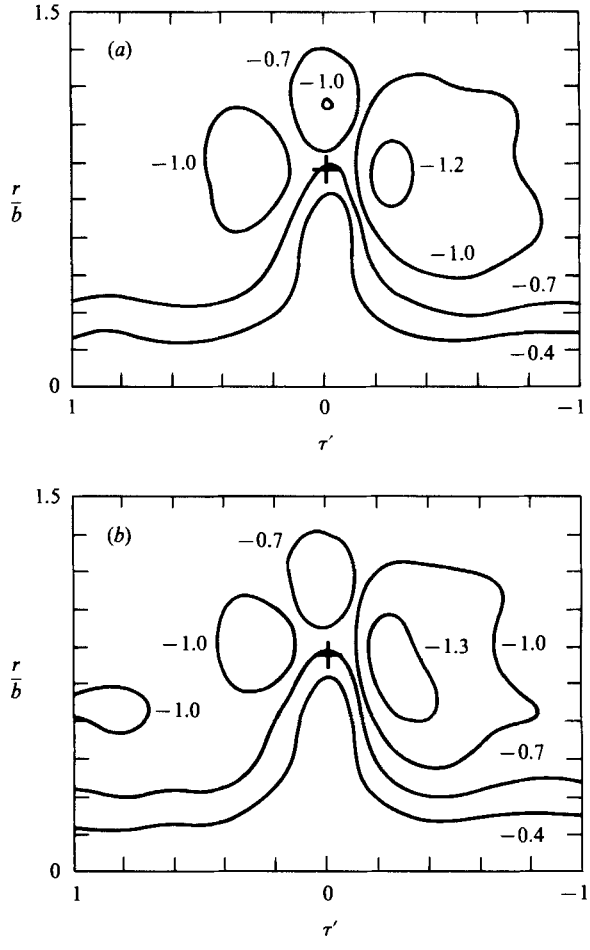

FIGURE 16. Contours of $2\langle s\rangle/|\partial\bar{u}/\partial r|_{\max}$: (*a*) mode +1; (*b*) mode −1. $\langle s\rangle = \frac{1}{2}(\partial\langle v\rangle/\partial x + \partial\langle u\rangle/\partial r)$.

side. Large shear strain rate means strong structure distortion; as the negative value of the shear strain rate suggests, the distortion is in a direction inclined to the jet upstream. This causes more transfer of energy from the structure to the small-scale motions on the downstream side, as evident in the distribution of the turbulence production term $-\langle u_r v_r\rangle\langle s\rangle$ shown in figure 17. These small-scale motions, in turn, should be responsible for the local active mixing.

The above results suggest that the mixing process inside the structure is not uniform – it is strongest on the downstream side. Therefore, one may speculate that the fluid on the upstream side of the structure, containing newly engulfed ambient potential fluid, will circulate around the structure to the downstream side and experience its most active momentum exchange between vortical and non-vortical motions (owing to the peak of $-\langle u_r v_r\rangle$ there). This mixed fluid later circulates to the upstream side, collects new ambient fluid, and moves again to the downstream side for another turn of active mixing, and so on. This proposed mixing mechanism, although plausible, remains somewhat conjectural, as the spatial resolution of the ×-wire rake is not sufficient for detailed investigation of small-scale motions.

In figure 15, there is another high-Reynolds-stress region on the far left side. The

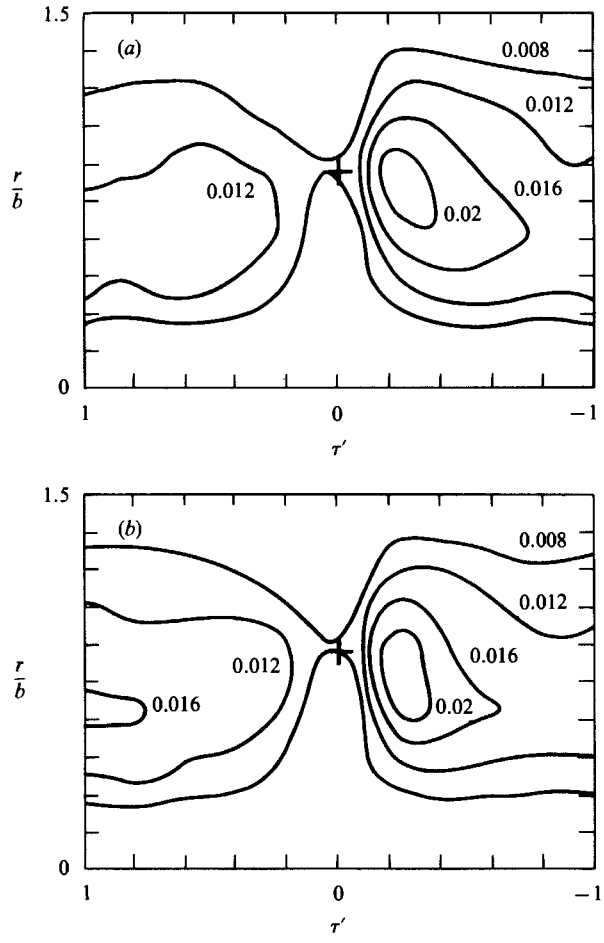

FIGURE 17. Contours of $\langle p\rangle/U_m^2|\partial\bar{u}/\partial r|_{max}$: (*a*) mode +1; (*b*) mode −1. $\langle p\rangle = -2\langle u_r v_r\rangle\langle s\rangle$.

above discussions, however, do not refer to this. At a distance this far away from the vorticity peak, which is the detection reference, the measured Reynolds stress can be affected significantly by the jitters of large-scale motions with respect to the detection reference and dissimilarities among individual large-scale structures. This does not suggest that there is no active mixing there. In fact, a similar result in the plane mixing layer was proved to be related to the separatrix region where secondary streamwise vortices (or ribs) were observed (Konrad 1976; Bernal & Roshko 1986). Hopefully, further work aligning successive realizations in the substructure region in between primary structures will shed light on this issue.

3.5. *Self-similarity of helical structures*

The preceding discussions have shown the dominance and dynamical behaviour of the helical structures at $x/D = 50$. Whether these findings hold throughout the fully developed region is a basic issue and depends solely upon the similarity of the ensemble-averaged measures of the helical structures.

This issue was examined by comparing the timescale T and the contours of $\langle\Omega\rangle$, $\langle uv\rangle$ and $-\langle u_r v_r\rangle$ of the helical structures at $x/D = 100$ to those measured at

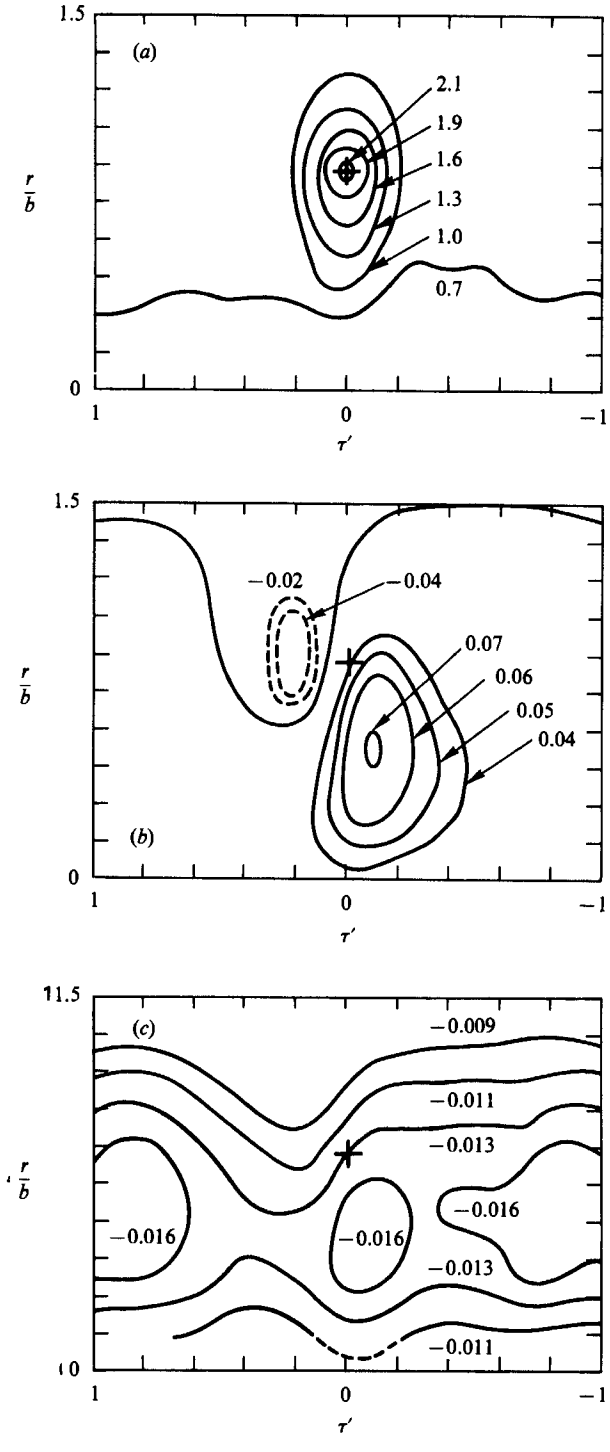

FIGURE 18. Contours of mode +1 structure at $x/D = 100$: (*a*) $\langle \Omega \rangle / |\partial \bar{u}/\partial r|_{\max}$; (*b*) $\langle uv \rangle / U_m^2$; (*c*) $-\langle u_r v_r \rangle / U_m^2$.

$x/D = 50$. The timescale T at $x/D = 100$, when non-dimensionalized by the local timescale $2b/U_m$, has a value of about 2.3, which is close to the value 2.4 obtained at $x/D = 50$. Observe that T, as seen in figure 3(*b*), corresponds to the wavelength λ of the helical mode, indicating that the structures at $x/D = 50$ and 100 are similar in their configurations. As seen in figure 18(*a–c*), the contours of $\langle \Omega \rangle$ and $\langle uv \rangle$ at $x/D = 100$ agree well with those at $x/D = 50$; however, the agreement on $-\langle u_r v_r \rangle$ is poorer (as in the conventional measurements done by Wygnanski & Fiedler 1969) but mostly in regions far away from the vorticity peak. This means that the helical structures at $x/D = 50$ and 100 are similar in their dynamical behaviour.

In the above comparison, the scales used, which include the half-radius b, the centreline velocity U_m, and the maximum mean shear $|\partial \bar{u}/\partial r|_{max}$ are all defined on the basis of the local mean velocity profile. They are the same scales used in asserting the self-similarity in conventional measurements This is also the case in the fully developed plane mixing layer where earlier measurements (Browand & Troutt 1980; Hussain & Zaman 1982) have shown the invariance of the structure configuration, recurrence frequency, and dynamics. The self-similarity of the mean flow may simply be the consequence of the self-similarity of the dominant structures.

4. Concluding remarks

The most important conclusion reached in this study is that, among the large-scale vortical structures examined in the fully developed region of a turbulent axisymmetric jet, there is a preferred helical configuration. While structures of axisymmetric and double-helical configurations also occur in the same flow region, the helical structures are the most dominant. This makes it meaningful to study turbulent transport in terms of the helical structures, and perhaps even to model the jet far field, at least to the first order, with the helical structures.

Experimental evidence in this investigation showed that the helical structure has a strong radial outward movement. This radial movement increases the induced speed of ambient fluid. In conjunction with the simultaneous local ejection of turbulent fluid and subsequent engulfment of ejected fluid with ambient fluid, it may be a major mechanism for momentum transfer and jet spreading. The evidence also suggests that the small-scale mixing process within the structure is most active on its downstream side, where the structure experiences a strong distortion inclined to the jet upstream.

That the helical structure was found to be the dominant structure provides one more piece of support for the linear stability analysis, which predicted the helical mode to be the most unstable mode for the jet far-field mean velocity profile (Batchelor & Gill 1962; Morris 1976). Beyond this, the linear analysis has certain limitations in describing the nonlinear structure dynamics and evolution of helical structures (Hussain 1980; Strange & Crighton 1983). Moreover, the use of the mean velocity profile as the basic flow imposes a major constraint in predicting the structure behaviour. In this study, for instance, the phenomenon of switching among different modes of structures, which should be related to the instantaneous flow dynamics, is unlikely to be explained by the analysis of the time-mean profile. Nonetheless, knowing this limit, the linear analysis has proved to be a useful guide in coherent-motion studies.

This study was based on the simple idea of using large-scale vorticity peaks as detection references to sample and analyse the large-scale vortical structures. The scheme, also applicable to other turbulent shear flows, can be improved in several

ways. One can refine its space and time resolutions. This would be essential to the investigation of the configuration and dynamics of the substructures associated with the three-dimensional helical structures. The substructures are expected to be more complex than the longitudinal vortices or ribs of the presumably two-dimensional rolls in the plane mixing layer. The scheme can also include alignment in the time axis or even in the radial directions when more vorticity sensors are available. This can produce dividends in understanding the flow physics, as proved for instance by Hayakawa (1985) in the plane wake flow.

The authors are indebted for helpful discussions to Drs S. J. Kleis and P. Bandyopadhyay during the research work, and to Professors F. K. Browand, C. M. Ho, and Dr A. S. Hersh during the preparation of this paper. This work was supported by the National Science Foundation Grant NSF MEA 81-11676.

REFERENCES

Batchelor, G. K. & Gill, A. E. 1962 Analysis of the stability of axisymmetric jets. *J. Fluid Mech.* **14**, 529–551.

Bernal, L. P. & Roshko, A. 1986 Streamwise vortex structure in plane mixing layers. *J. Fluid Mech.* **170**, 499–525.

Blackwelder, R. F. & Kaplan, R. E. 1976 On the wall structure of the turbulent boundary layer. *J. Fluid Mech.* **76**, 89–112.

Browand, F. K. & Troutt, T. R. 1980 A note on spanwise structure in the two-dimensional mixing layer. *J. Fluid Mech.* **97**, 771–781.

Browand, F. K. & Weidman, P. D. 1976 Large scales in the developing mixing layer. *J. Fluid Mech.* **76**, 127–144.

Cantwell, B. J. 1981 Organized motion in turbulent flow. *Ann. Rev. Fluid Mech.* **13**, 457–515.

Chevray, R. & Tutu, N. K. 1978 Intermittency and preferential transport of heat in a round jet. *J. Fluid Mech.* **88**, 133–160.

Coles, D. 1981 Prospects for useful research on coherent structure in turbulent shear flow. *Proc. Indian Acad. Sci.* **4**, 111–128.

Crow, S. C. & Champagne, F. H. 1971 Orderly structure in jet turbulence. *J. Fluid Mech.* **48**, 547–591.

Dimotakis, P. E., Miake-lye, R. L. & Papantoniou, D. A. 1983 Structure and dynamics of round turbulent jets. *Phys. Fluids* **26**, 3185–3192.

Gupta, A. K., Laufer, J. & Kaplan, R. E. 1971 Spatial structure in the viscous sublayer. *J. Fluid Mech.* **50**, 493–512.

Hayakawa, M. 1985 Eduction of coherent structures in the turbulent plane wake. In *Proc. 5th Symp. on Turbulent Shear Flows, Cornell University*, pp. 433–438. Springer.

Hussain, A. K. M. F. 1980 Coherent structures in perturbed and unperturbed jets. In Lecture Notes in Physics, vol. 136, pp. 252–291. Springer.

Hussain, A. K. M. F. & Clark, A. R. 1981*a* Measurements of wavenumber celerity spectrum in plane and axisymmetric jets. *AIAA J.* **19**, 51–55.

Hussain, A. K. M. F. & Clark, A. R. 1981*b* On the coherent structure of the axisymmetric mixing layer: a flow-visualization study. *J. Fluid Mech.* **104**, 262–294.

Hussain, A. K. M. F. & Zaman, K. B. M. Q. 1982 The organized motions in the turbulent plane mixing layer. *Rep.* FM-14. University of Houston. See also *J. Fluid Mech.* **159**, 85 (1985).

Kibens, V. 1980 Discrete noise spectrum generated by an acoustically excited jet. *AIAA J.* **18**, 434–441.

Konrad, J. H. 1976 An experimental investigation of mixing in two-dimensional turbulent shear flows with applications to diffusion limited chemical reactions. *Intern. Rep.* CIT-8-PU. California Institute of Technology.

LIN, C. C. 1953 On Taylor's hypothesis in wind tunnel turbulence. *Q. Appl. Maths* **10**, 295–306.

LUMLEY, J. L. 1981 Coherent structures in turbulence. In *Transition and Turbulence* (ed. R. E. Meyer), pp. 215–242. Academic.

MORRIS, P. J. 1976 The spatial viscous instability of axisymmetric jets. *J. Fluid Mech.* **77**, 511–529.

OSHIMA, Y. & ASAKA, S. 1977 Interaction of two vortex rings along parallel axes in air. *J. Phys. Soc. Japan* **42**, 708–713.

REYNOLDS, A. J. 1962 Observations of a liquid-into-liquid jet. *J. Fluid Mech.* **14**, 552–556.

SREENIVASAN, K. R. 1984 The azimuthal correlations of velocity and temperature fluctuations in an axisymmetric jet. *Phys. Fluids* **27**, 867–875.

STRANGE, P. J. R. & CRIGHTON, D. G. 1983 Spinning modes on axisymmetric jets. *J. Fluid Mech.* **134**, 231–245.

TSO, J. 1983 Coherent structures in a fully-developed turbulent axisymmetric jet. Ph.D. thesis, Johns Hopkins University.

TSO, J., KOVASZNAY, L. S. G. & HUSSAIN, A. K. M. F. 1981 Search for large-scale coherent structures in the nearly self-preserving region of a turbulent axisymmetric jet. *Trans. ASME* I: *J. Fluids Engng* **103**, 503–508.

WYGNANSKI, I. & FIEDLER, H. 1969 Some measurements in the self-preserving jet. *J. Fluid Mech.* **38**, 577–612.

ZAMAN, K. B. M. Q. & HUSSAIN, A. K. M. F. 1980 Vortex pairing in a circular jet under controlled excitation: part 1, general jet response. *J. Fluid Mech.* **101**, 449–491.

ZAMAN, K. B. M. Q. & HUSSAIN, A. K. M. F. 1981 Taylor hypothesis and large-scale coherent structures. *J. Fluid Mech.* **112**, 379–396.